https://dx.doi.org/10.1016/j.jcsr.2020.106078

Material properties and residual stresses of cold-formed octagonal hollow sections

Junbo Chen[1,2], Haixin Liu[1,2], Tak-Ming Chan[1,2]*

[1] Department of Civil and Environmental Engineering, The Hong Kong Polytechnic University, Hung Hom, Hong Kong, China

[2] Chinese National Engineering Research Centre for Steel Construction (Hong Kong Branch), The Hong Kong Polytechnic University, Hung Hom, Hong Kong, China

*Corresponding author: tak-ming.chan@polyu.edu.hk

Abstract: This paper presents an experimental investigation on the material properties and residual stress distributions in cold-formed steel octagonal hollow sections. Octagonal hollow sections (OctHSs) manufactured through two fabrication routes were considered. Two batches of steel plates with measured yield strengths of 546.5 MPa and 580.7 MPa were employed. A total of 46 tensile coupons taken from the parent plates and cold-formed hollow tubes were tested to obtain the material properties of parent metals and to assess strength variations within the sections caused by press-braking and welding process. A new bilinear plus nonlinear strain-hardening material model was proposed for the materials at flat regions and an existing material model for cold-formed steel was adopted for the materials at corners. These models yielded satisfactory agreements with the test results in terms of stress-strain relationships. Up to date, investigations on the residual stress distributions in cold-formed OctHSs remain limited. Subsequently, residual stress measurements on 4 cold-formed octagonal hollow sections with different fabrication routes and different flat side width-to-thickness ratios were performed. Sectioning method was adopted in this study with 74 strips extracted and more than 800 strain readings taken. Results of residual stress magnitudes and distributions are presented and discussed. Membrane residual stresses were typically found to be as high as 62% of the material yield strength, whilst bending residual stresses were found to be below 39% of the material yield strength. Simplified models for the residual stress magnitudes and distributions in the cold-formed octagonal hollow sections were proposed on the basis of test results.

Keywords: Material properties; Residual stresses; Cold-formed; Octagonal hollow sections.

1. Introduction

Tubular structural members have been widely adopted in civil structural applications owing to their structural efficiency and aesthetic appearance [1]. Numerous experimental and numerical investigations on tubular members with circular hollow sections (CHSs), elliptical hollow sections (EHSs), square hollow sections (SHSs) and rectangular hollow sections (RHSs) in both normal strength steel and high strength steel have been undertaken [2-6]. Design rules for steel hollow sections have been published worldwide such as EN 1993-1-1 [7], AISC 360-16 [8], and AISI S100-16 [9]. In recent years, steel polygonal hollow sections, in particular octagonal hollow

sections (OctHSs), have attracted significant attention from architects, structural engineers and researchers [10-17], and have been utilised in civil applications such as transmission poles, antennas and lighting structures [12, 17]. Example of an OctHS lighting column is depicted in Fig. 1. An obvious attraction of OctHSs is that the flat side width of the plate element is smaller than square counterparts with the same perimeter. OctHSs therefore exhibit stronger local buckling resistance than that of SHSs/RHSs [16-17]. In addition, OctHSs provide flat surfaces for easier beam-to-column connection constructions as compared with CHSs [16].

For cold-formed hollow sections, unlike plate products and built-up sections, the cold-forming processes such as cold-rolling and press-braking alter the material properties within the hollow section when compared to parent metal [18]. Hence, the material properties can differ from part to part within the hollow section. One important reason causing the variation of the material properties is the plastic deformation at the cold-formed regions which leads to excessive plastic strain, resulting in strain-hardening [16, 18]. Moreover, welding process introduces heat energy to the weld metal which also influences the material properties around the welding seam and causes heat affected zone (HAZ). Material properties within HAZ can be different from those of the materials outside HAZ [19, 20]. The non-uniform thermal and plastic strains also result in residual stresses within the hollow section. Residual stresses within the hollow section affect the structural behaviours of the members by causing premature yielding through part of the material thickness, which may further lead to instability in compression members [21, 22]. Without good understanding of the variation of the material properties and the residual stresses within hollow sections, inaccurate predictions of the structural performance might be obtained. To date, tremendous amount of investigations, both experimentally and numerically, have been carried out regarding OctHSs on material properties, residual stresses, and stabilities [10-17]. However, for cold-formed OctHSs, investigations on material properties at corner regions and measurements on residual stresses are rather limited. Fang et al. [16] experimentally investigated the variation of material properties and residual stresses of OctHSs manufactured from S690 steel plates. Three different fabrication routes were used. Zhu et al. [17] carried out experimental tests on the material properties, residual stresses and stub column behaviour of OctHSs focusing on S355 steel plates. In [17], only one fabrication route was considered. Studies incorporating 460 steel are scarce, potentially inhibiting attempts to develop effective design recommendations for OctHSs. Therefore, for the purpose of developing design guidelines for OctHSs, it is of vital significance to thoroughly investigate the material properties and residual stresses of cold-formed OctHSs using 460 steel plates.

The material properties and residual stresses of cold-formed OctHSs manufactured from 460 steel plates were investigated herein. A total of 46 coupon tests consisting of flat coupons, corner coupons and weld coupons were conducted. Due to cold-forming process, strength enhancement was observed at corner regions. Essentially unchanged material properties were observed in the

flat regions when compared to parent metals. Existing material models for hot-rolled steel and cold-formed steel were discussed and parameters for predicting stress-strain curves at flat and corner portions were given. Residual stress measurements on four OctHS specimens were carried out. Distributions of the residual stress were presented and discussed. Simplified predictive models for the residual stress distributions were then proposed.

2. Material property investigations

2.1 General

In order to investigate the effect of fabrication process on the material properties of cold-formed octagonal hollow sections (OctHSs), tensile coupons were extracted from parent plates, flat and corner portions of hollow tubes. Two batches of steel plates with nominal yield strength of 460 MPa and with nominal thicknesses of 3 mm and 6 mm were employed in the study. To form an OctHS, normally there are three fabrication routes: (1) welding two cold-formed half-sections at two corners, (2) welding two cold-formed half-sections at two flat surfaces and (3) welding eight flat plates, as discussed in [16]. As this study focuses on cold-formed sections, fabrication routes (1) and (2) were adopted, denoted as CF1 and CF2 respectively as shown in Fig. 2. The former has three cold-bent corners in one cold-formed half-section, while the latter has four cold-bent corners. The difference between these two fabrication routes was the location of the welding seam.

2.2 Tensile coupon tests

To obtain the material properties, some 46 tensile coupon tests were conducted: 6 flat coupons taken from parent plates (3 for each plate), 28 flat coupons extracted from flat portions of cold-formed hollow tubes, 8 corner coupons removed from the corner portions, and 4 coupons cut from welding seams. All the coupon tests were carried out in accordance with EN ISO 6892-1:2016 [23] using an in-house Instron 8803 fatigue testing system with a capacity of 500 kN. Electrical strain gauges were affixed at the mid-length of both sides of the tensile coupons. In addition, an extensometer with the extensometer gauge length of either 25 mm or 50 mm was used to record full engineering stress-strain responses. The extensometer elongation at fracture $\varepsilon_{f,25}$ or $\varepsilon_{f,50}$ was directly captured by the 25 mm or 50 mm extensometer attached on the coupons. According to EN ISO 6892-1:2016, proportional elongation at fracture ε_f is based on an original gauge length of $5.65\sqrt{A_0}$, where A_0 is cross-sectional area within the original gauge length of the coupon. In this study, if the original gauge length of the coupon is approximately equal to 25 mm or 50 mm (extensometer gauge length), ε_f was directly obtained by the final strain reading of corresponding extensometer; otherwise, it was determined by carefully fitting the fractured pieces and comparing the proportional gauge length after fracture to the original proportional gauge length. For each coupon, the original proportional gauge length was initially marked by fine lines. During each

tensile coupon test, the loading was paused twice near yield and ultimate strength for 120 s for stress relaxation to obtain the static stress-strain curves [24]. The obtained static stress-strain curves were then used to determine the static material properties, such as yield strength and ultimate strength.

2.2.1 Parent plate coupon tests

Material properties of parent metals were first measured by flat tensile coupon tests. Three coupons were taken from each batch of the parent plates. To measure the Poisson's ratio, four strain gauges were mounted at the mid-length of each tensile coupon, with two mounted in longitudinal direction and the other two in transverse direction. The test arrangement of flat tensile coupon tests is shown in Fig. 3. The mean measured material properties of parent plates are summarised in Table 1, where $E_{s,p}$ is elastic modulus of steel, v is Poisson's ratio, $f_{y,p}$ is yield strength, $f_{u,p}$ is ultimate strength, $\varepsilon_{sh,p}$ is strain-hardening strain (the strain at which strain-hardening initiates), $\varepsilon_{u,p}$ is strain at the ultimate strength, $\varepsilon_{f,25p}$ or $\varepsilon_{f,50p}$ is elongation at fracture determined by a 25 mm or 50 mm extensometer, and $\varepsilon_{f,p}$ is proportional elongation at fracture. The letter "p" in the subscript of the symbols indicates parent metal. Typical full stress-strain curves of the tensile coupons taken from each parent metal are presented in Fig. 4.

2.2.2 Quarter-section coupon tests

As discussed in Section 1, manufacturing process affects the material properties within the hollow section. To examine the variation of the material properties, tensile coupons were extracted from a quarter-section. This is based on an assumption that the effect of manufacturing process is doubly symmetric due to geometric symmetry. A total of 4 cold-formed OctHSs, namely CF1-75×3, CF1-75×6, CF2-75×3 and CF2-75×6, were chosen. The designation of the specimens firstly gives the fabrication route which is followed by nominal cross-sectional size (flat side width by thickness). The mean measured cross-sectional dimensions of the 4 sections are reported in Table 2. For each cold-formed section, a total of 10 coupons were extracted from different locations within a quarter-section. One coupon was cut from the welding seam to obtain the material properties of the weld metal, one coupon was removed at the location 10 mm away from the centre line of the welding seam to investigate the effect of welding process, and the remaining 8 coupons were taken successively in the remaining portion to check the variation of material properties with the section. The locations where the coupons were extracted are depicted in Fig. 5.

For all the quarter-section coupon tests, a 25 mm gauge length extensometer was used to capture the full stress-strain responses and two strain gauges were attached at the mid-length on both sides of the coupon to measure the elastic modulus of the coupon. All flat coupons had a width of 5 mm along the 25 mm extensometer gauge length. The width of all the corner coupons along the parallel

length was 4 mm to minimise the load eccentricity introduced during the testing process. For the coupons that the original gauge length is not approximately equal to 25 mm (extensometer gauge length), a series of fine lines were marked on the coupon surface to capture the elongation at fracture ε_f after the test. It was observed that the corner coupons curved after removal, which is due to the release of the through-thickness residual stress. No attempt was made to straighten the coupons prior to testing. Two 10 mm diameter holes were drilled on both ends of the corner coupons and a pair of specially grips with two pins were used to avoid load eccentricity. Test arrangements of flat and corner tensile coupons taken from hollow tubes are demonstrated in Fig. 6. The measured material properties of the 4 quarter-section coupons are reported in Tables 3-6, in which E_s is elastic modulus, f_y is yield strength (taken as lower yield strength for steel exhibiting yield plateau or 0.2% proof strength for steel with rounded stress-strain relationship), f_u is ultimate strength, ε_u is strain at the ultimate strength, $\varepsilon_{f,25}$ is elongation at fracture determined by a 25 mm extensometer, and ε_f is proportional elongation at fracture. Typical stress-strain curves of flat and corner coupons extracted from a hollow tube are shown in Fig. 7. Tensile coupons taken from the quarter-section of CF1-75×3 are shown in Fig 8. The distributions of measured yield strength and ultimate strength in CF1-75×3, CF1-75×6, CF2-75×3 and CF2-75×6 are presented in Figs. 9-12 respectively.

Essentially similar stress-strain responses were observed for the flat and corner coupons of each steel batch. The mean measured material properties of flat coupons are reported in Table 7, in which $E_{s,f}$ is elastic modulus, $f_{y,f}$ is yield strength, $f_{u,f}$ is ultimate strength, $\varepsilon_{u,f}$ is strain at the ultimate strength, $\varepsilon_{f,25f}$ is elongation at fracture determined by a 25 mm extensometer, and $\varepsilon_{f,f}$ is proportional elongation at fracture. The letter "f" after comma in the subscript denotes flat coupons cut from hollow tubes. Similarly, the mean measured material properties of corner coupons are listed in Tables 8, where $E_{s,c}$ is elastic modulus, $f_{y,c}$ is yield strength (taken as 0.2% proof strength), $f_{u,c}$ is ultimate strength, $\varepsilon_{u,c}$ is strain at ultimate strength, $\varepsilon_{f,25c}$ is elongation at fracture determined by the 25 mm extensometer, and $\varepsilon_{f,c}$ is proportional elongation at fracture. The letter "c" in the subscript designates corner coupons extracted from hollow tubes. It was observed, by comparing the material properties in Tables 7-8 to that of parent plates (Table 1), that the fabrication routes of combined press braking and welding produces essentially unchanged properties in the flat regions, but causes large strength enhancements at the corners which is the result of excessive strain-hardening. It was noted that the strength enhancement is accompanied by a reduction of ductility.

2.3 Strength enhancement at corner region

The coupon test results reported in Section 2.2 reveal that the yield strength of the corner portions is greatly enhanced due to the pronounced strain-hardening. The strength enhancement ratios, which is defined as the corner yield strength over flat yield strength ratio $f_{y,c} / f_{y,f}$, of the 3 mm and 6 mm steel are 1.21 and 1.27, respectively. Karren [25] suggested that the influence of the strength

197 enhancement at cold-formed regions should be taken into account in calculations of cross-section
198 resistance. A predictive model for the strength enhancement was then proposed for press-braked
199 and cold-rolled sections by Karren [25], as given in Eq. (1). This model has been standardised in
200 AISI S100-16 [9]. To further assess the applicability of this model to cold-formed OctHSs, a
201 database composed of 26 corner coupon test results reported in [16, 17] and this study was
202 developed. All the corner coupons were extracted from cold-formed OctHSs fabricated by a
203 combination of press-braking and welding. Three steel grades, namely 355, 460 and 690, were
204 covered with the yield strength ranging from 373 MPa to 810 MPa. This predictive model
205 reasonably predicts the strength enhancement, yielding a mean prediction-to-test value of 1.03
206 with a corresponding CoV (coefficient of Variance) of 0.04. The assessment of the predictive
207 model is presented in Fig. 13.
208

$$\frac{f_{\mathrm{y,c}}}{f_{\mathrm{y,p}}}=\frac{B_{\mathrm{c}}}{(r_{\mathrm{i}}/t)^{\mathrm{m}}} \tag{1}$$

209 where

$$B_{\mathrm{c}}=3.69\frac{f_{\mathrm{u,p}}}{f_{\mathrm{y,p}}}\text{-}0.819\left(\frac{f_{\mathrm{u,p}}}{f_{\mathrm{y,p}}}\right)^{2}\text{-}1.79$$

$$m=0.192\frac{f_{\mathrm{u,p}}}{f_{\mathrm{y,p}}}\text{-}0.068$$

210

211 ***2.4 Material models***

212

213 With the advancements of finite element modelling (FEM) techniques, some commercial finite
214 element packages such as ABAQUS [26] are capable of replicating steel behaviour under
215 extremely large strain. Precise stress-strain models up to ultimate strength are of great importance
216 for FEM to capture behaviours of steel members like beam. This section briefly reviews the
217 existing material models for hot-rolled and cold-formed steels as they can be used to describe the
218 material properties at flat and corner regions respectively. Parameters for obtaining stress-strain
219 curves are then given.

220

221 *2.4.1 Hot-rolled material model*

222

223 The hot-rolled structural steel normally exists a linear elastic range and a sharply defined yield
224 point followed by a pronounced plastic yield plateau. For a description of the stress-strain
225 behaviour of hot-rolled structural steel, a three-stage nonlinear model (bilinear plus nonlinear
226 hardening model) was proposed by Yun and Gardner [27] on a basis of a coupon test database
227 comprising over 500 samples. This model is expressed as follows:
228

$$\sigma = \begin{cases} E_s\varepsilon & \text{for } \varepsilon \le \varepsilon_y \\ f_y & \text{for } \varepsilon_y < \varepsilon \le \varepsilon_{sh} \\ f_y + \left(f_u - f_y\right)\left[0.4\varepsilon_x + 2\varepsilon_x / \left(1 + 400\varepsilon_x{}^5\right)^{1/5}\right] & \text{for } \varepsilon_{sh} < \varepsilon \le \varepsilon_u \ \left(\varepsilon_x = \dfrac{\varepsilon - \varepsilon_{sh}}{\varepsilon_u - \varepsilon_{sh}}\right) \end{cases} \quad (2)$$

where E_s is elastic modulus, f_y is yield strength, f_u is ultimate strength, ε_y is yield strain, ε_{sh} is strain-hardening strain, ε_u is ultimate strain at ultimate strength. If ε_{sh} and ε_u are not reported, they could be determined by empirical equations as expressed in Eqs. 3 and 4 [27].

$$\varepsilon_{sh} = 0.1\frac{f_y}{f_u} - 0.055 \quad \text{but } 0.015 \le \varepsilon_{sh} \le 0.03 \quad (3)$$

$$\varepsilon_u = 0.6(1 - \frac{f_y}{f_u}) \quad \text{but } \varepsilon_u \ge 0.06 \quad (4)$$

It is noted that the shape of the stress-strain curve in the nonlinear strain-hardening range is similar to that of initial part of Ramberg-Osgood model up to the 0.2% proof strength, as shown in Fig. 14 and 15. Hence, it is proposed herein to use a modified Ramberg-Osgood model to describe the stress-strain behaviour of the nonlinear strain-hardening range. The modified Ramberg-Osgood model is obtained by a linear transformation of the stress and strain in the strain-hardening range from point (ε_{sh},f_y) to the origin, as given in Eq. 5, in which $\varepsilon^* = \varepsilon - \varepsilon_{sh}$, $\sigma^* = \sigma - f_y$, $f_u^* = f_u - f_y$, $E^* = E_{sh}$, $\varepsilon_p^* = \varepsilon_u - \varepsilon_{sh} - (\sigma - f_y)/E_{sh}$ and m is the strain-hardening exponent. Commencing at the strain-hardening point, the modified Ramberg-Osgood model can be expressed by Eq. 6, in which E_{sh} is the initial slope of the stress-strain curves in the strain-hardening range, termed as hardening modulus. E_{sh} can be directly obtained from material tests. If the value is not reported, an equation (see Eq. 7) proposed in [27] might be used to determine the value.

$$\varepsilon^* = \frac{\sigma^*}{E^*} + \varepsilon_p^*\left(\frac{\sigma^*}{f_u^*}\right)^m \quad (5)$$

$$\varepsilon - \varepsilon_{sh} = \frac{\sigma - f_y}{E_{sh}} + \left(\varepsilon_u - \varepsilon_{sh} - \frac{f_u - f_y}{E_{sh}}\right)\left(\frac{\sigma - f_y}{f_u - f_y}\right)^m \quad (6)$$

$$E_{sh} = \frac{f_u - f_y}{0.4(\varepsilon_u - \varepsilon_{sh})} \quad (7)$$

Hence a full range material model can be obtained by combining the bilinear model in Eq. 2 with the modified Ramberg-Osgood model for nonlinear strain-hardening range as given in Eq. 8.

$$\text{(1) Bilinear: } \sigma = \begin{cases} E_s \varepsilon & \text{for } \varepsilon \le \varepsilon_y \\ f_y & \text{for } \varepsilon_y < \varepsilon \le \varepsilon_{sh} \end{cases}$$
$$\text{(2) nonlinear: } \varepsilon = \varepsilon_{sh} + \frac{\sigma - f_y}{E_{sh}} + \left(\varepsilon_u - \varepsilon_{sh} - \frac{f_u - f_y}{E_{sh}} \right) \left(\frac{\sigma - f_y}{f_u - f_y} \right)^m \quad \text{for } \sigma > f_y \tag{8}$$

To make direct comparisons, a constant *m* value of 6.0 was firstly used. Representative comparisons of the nonlinear hardening stress-strain curves between the proposed predictive model and test results reported in [16, 17] and this study are shown in Fig. 16. It can be seen from Fig. 16 (a) to (c) that the proposed model yields a better prediction of the material responses than the model proposed by Yun and Gardner [27]. For the S690 test in [16], the result of the proposed model is significantly improved by changing the *m* value from 6.0 to 3.0 (see Fig. 17). A possible reason for this phenomenon is that the exponent *m* is related to the yield strength and ultimate strength of the materials. An empirical equation to predict the value of *m* might be derived based on a large size of test database.

2.4.2 Cold-formed material model

Unlike hot-rolled steel, cold-formed steel generally exhibits a rounded stress-strain relationship, which is similar in shape to stainless steel. In this case, 0.2% proof strength $f_{0.2}$ is frequently used as an equivalent yield strength. Adopting 0.2% proof strength and corresponding strain in the original form of Ramberg-Osgood expression, Eq. 9 can be obtained [28]. This equation performs well in predicting stress-strain curves up to 0.2% proof strength but tends to overestimate the material responses after the yield point [29].

$$\varepsilon = \frac{\sigma}{E_s} + 0.002 \left(\frac{\sigma}{f_{0.2}} \right)^n \tag{9}$$

It is noted that the stress-strain curve in the range between 0.2% proof strength and ultimate strength is similar in shape to the initial range up to 0.2% proof strength [29]. A two-stage full range stress-strain curve was then proposed and could be written out as Eq. 10,

$$\varepsilon = \begin{cases} \dfrac{\sigma}{E_s} + 0.002 \left(\dfrac{\sigma}{f_{0.2}} \right)^n & \text{for } \sigma \le f_{0.2} \\ \dfrac{\sigma - f_{0.2}}{E_{0.2}} + \left(\varepsilon_u - \varepsilon_{0.2} - \dfrac{f_u - f_{0.2}}{E_{0.2}} \right) \left(\dfrac{\sigma - f_{0.2}}{f_u - f_{0.2}} \right)^m + \varepsilon_{0.2} & \text{for } \sigma > f_{0.2} \end{cases} \tag{10}$$

where n and m are strain-hardening exponents in the first stage and second stage respectively and can be obtained by Eq. 11 and 12, $E_{0.2}$ is tangential modulus of elasticity at 0.2% proof strength and is given in Eq. 13, and $\varepsilon_{0.2}$ is total strain at 0.2% proof strength. In Eq. 11, $f_{0.01}$ is 0.01% proof strength.

$$n = \frac{\ln(20)}{\ln(f_{0.2} / f_{0.01})} \tag{11}$$

$$m = 1 + 3.5\frac{f_{0.2}}{f_{\mathrm{u}}} \tag{12}$$

$$E_{0.2} = \frac{E_{\mathrm{s}}}{1 + 0.002nE_{\mathrm{s}} / f_{0.2}} \tag{13}$$

It is found in [30] that using the 0.05% proof strength $f_{0.05}$ instead of 0.01% proof strength to determine the strain-hardening exponent n provides a better prediction of stainless steel stress–strain curves. Hence Eq. 14 could be used to replace Eq. 11.

$$n = \frac{\ln(4)}{\ln(f_{0.2} / f_{0.05})} \tag{14}$$

It was found by Ma et al. [22] that the strain-hardening exponent n increased with the increase in plastic strain ε_{p}. A new model, in which the strain-hardening exponent n_{pro} is formulated as a function of plastic strain, was proposed, as expressed in Eq. 15,

$$n_{\mathrm{pro}} = f\left(\varepsilon_{\mathrm{p}}\right) = n + K\varepsilon_{\mathrm{p}}^{m} \tag{15}$$

where n is the original strain-hardening exponent, m and K are the exponent and coefficient for calculating n_{pro}, ε_{p} is plastic strain. The coefficient K is determined by modulus of elasticity, 0.2% proof strength, ultimate strength and strain at ultimate strength by Eq. 16. The exponent m is obtained by try and error analysis fitting the predicted curve to the test results. The plastic strain is equal to total strain minus elastic strain. Hence, Eq. 17 is obtained.

$$K = \left[\log_{f_{\mathrm{u}}/f_{0.2}}\left(\frac{\varepsilon_{\mathrm{u}} - f_{\mathrm{u}} / E_{\mathrm{s}}}{0.002}\right)\right] / \left(\varepsilon_{\mathrm{u}} - f_{\mathrm{u}} / E_{\mathrm{s}}\right)^{m} \tag{16}$$

$$\varepsilon_{\mathrm{p}} = \varepsilon - \frac{\sigma}{E} = 0.002\left(\frac{\sigma}{f_{0.2}}\right)^{n_{\mathrm{pro}}} \tag{17}$$

Substituting Eq. 15 into Eq. 17, the explicit form of the proposed stress-strain model is given in Eq. 18. The stress-strain curve can be determined when the material parameters, namely elasticity

modulus, 0.01% proof strength (or 0.05% proof strength), 0.2% proof strength, ultimate strength, strain at ultimate strength and exponent *m*, are obtained.

$$\begin{cases} \sigma = \left(\dfrac{\varepsilon_{\mathrm{p}}}{0.002} \right)^{\left(\frac{1}{n + K\varepsilon_{\mathrm{p}}^{m}} \right)} f_{0.2} \\ \varepsilon = \varepsilon_{\mathrm{p}} + \dfrac{\sigma}{E_{\mathrm{s}}} = \varepsilon_{\mathrm{p}} + \dfrac{f_{0.2}}{E_{\mathrm{s}}} \left(\dfrac{\varepsilon_{\mathrm{p}}}{0.002} \right)^{\left(\frac{1}{n + K\varepsilon_{\mathrm{p}}^{m}} \right)} \end{cases} \tag{18}$$

The material parameters for corner coupons are summarised in Table 9. The comparisons of the stress-strain curves between the model predictions and test results are depicted in Fig. 18. The results of the comparisons indicate that the model proposed in [22] correlated well with test data.

3. Residual stress measurements

Residual stresses, which are introduced by manufacturing process, exist in both longitudinal and transverse directions of cold-formed steel members. The longitudinal residual stresses are more influential on the structural responses than that in transverse direction [16, 21]; hence, the focus of this study was put on the longitudinal residual stresses which has membrane and bending residual stress components (as shown in Fig. 19). There are various residual stress measurement techniques which are classified as destructive and non-destructive methods, such as neutron or electron diffraction, ultrasonic method and sectioning method. A comprehensive comparison of the different techniques is detailed in [31]. Sectioning method is a commonly used destructive method which determines residual stresses by measuring the deformation of strips extracted from cold-formed members. It has been extensively used to obtained residual stress distributions in structural steel [16, 17, 22] and stainless steel [21] sections. In this study, sectioning method was used.

3.1 Specimens

Sectioning was performed on four cold-formed OctHSs to quantify the longitudinal residual stresses namely membrane and bending residual stresses. Two fabrication routes, CF1 and CF2 as shown in Fig. 2, were adopted and two cross-sectional dimensions with nominal flat side width by thickness of 75×6 and 105×3 were chosen. The four specimens were labelled as CF1-75×6, CF1-105×3, CF2-75×6, and CF2-105×3. All the specimens prepared for measurements were 300 mm in length. A quarter of the sections was marked into longitudinal strips because of the symmetrical distribution of residual stresses. The widths of strips in the 75×6 and 105×3 sections were 10 mm and 12 mm, respectively. Strain gauges with a 5 mm gauge length were mounted onto both external and internal surfaces of the marked longitudinal strips at the mid-length of each strip. Each strain

gauge was carefully coated by water-proof tape to avoid any damage in the strain gauge during the sectioning process. The external and internal views of specimen CF2-75×6 are presented in Fig. 20.

Initial readings of the strain gauges on the external and internal surfaces were recorded (denoted as $\varepsilon_{ext,i}$ and $\varepsilon_{int,i}$, respectively) prior to the conduction of sectioning process. After the completion of the sectioning process, the residual stresses introduced by the manufacturing process within the cross-section were released. The readings of each strain gauge were taken again (indicated as $\varepsilon_{ext,f}$ and $\varepsilon_{int,f}$, respectively) for all the cut strips. For each strain gauge, three readings were taken, and the mean value was used for subsequent analyses. The residual strains at the external ε_{ext} and internal ε_{int} surfaces can be calculated by subtracting the initial readings from the final readings. The membrane and bending residual strains are subsequently determined by Eqs. 19 and 20. The residual stresses are then obtained by Hook's Law ($\sigma = E\varepsilon$). It should be noted that positive and negative values indicate tensile and compression residual stresses respectively.

$$\varepsilon_{m} = -\left(\frac{\varepsilon_{ext} + \varepsilon_{int}}{2}\right) = -\left(\frac{\varepsilon_{ext,f} - \varepsilon_{ext,i}}{2} + \frac{\varepsilon_{int,f} - \varepsilon_{int,i}}{2}\right) \tag{19}$$

$$\varepsilon_{b,ext} = -\varepsilon_{b,int} = -\left(\frac{\varepsilon_{ext} - \varepsilon_{int}}{2}\right) = -\left(\frac{\varepsilon_{ext,f} - \varepsilon_{ext,i}}{2} - \frac{\varepsilon_{int,f} - \varepsilon_{int,i}}{2}\right) \tag{20}$$

3.2 Results

The magnitudes and distributions of longitudinal residual stress in CF1-75×6, CF1-105×3, CF2-75×6, and CF2-105×3 were determined. Examples of deformed strips extracted from CF1-105×3 after sectioning are depicted in Fig. 21. The measured residual stresses were firstly normalised by the yield strength of parent metals. Then, the magnitudes and distributions of the normalised residual stresses including membrane residual stresses and bending residual stresses on the external surfaces are plotted with respect to the distance from welding seam, as demonstrated in Fig. 22. It was noted that OctHSs fabricated from different routes exhibited different distributions and magnitudes of residual stresses, indicating that the fabrication routes should be accounted for in the analysis. For the press-braked sections, the corner strips have larger curvatures than the others because of large bending residual stresses. This is because that the corner materials experienced pronounced plastic deformations during the fabrication process. The bending residual stresses at corners were typically found to be below $0.39f_{y,p}$ tensile stress on the external surface. The magnitudes of the bending residual stresses at the other locations were much lower than those of corners. In terms of maximum membrane residual stresses, the normalised values were found to be as $0.62f_{y,p}$ tensile stress, which were much higher than the bending residual stress amplitude.

The magnitudes of membrane residual stresses near the welding seam were greatly larger than other locations.

3.3 Simplified predictive models

The test results of the magnitudes and distributions of the membrane and bending residual stresses in cold-formed OctHSs were subsequently utilised to develop simplified predictive models. These models might be incorporated in structural analyses such as finite element modelling (FEM) to obtain better predictions in member behaviours. For easy application purpose, the distribution patterns were simplified as multi-linear curves with constant values at corner regions. Magnitudes of the residual stresses in the simplified models were obtained as the mean measured stresses at specific parts. Within the scope of this study, simplified predictive models for the longitudinal membrane and bending residual stress distributions in CF1 and CF2 sections (as shown in Fig. 2) were proposed. The distributions of the residual stresses are plotted over quarter-sections, as shown in Fig. 23.

The test results of residual stresses in cold-formed OctHS (CF2) manufactured from S355 steel in [17] is presented in Fig. 24(a). The yield strength of the S355 steel is 379 MPa. Simplified predictive models were derived based on the test results and the models are depicted in Fig. 24(b). Fang et al. [16] undertook residual stress measurements on OctHSs using S690 steel. Predictive models were also proposed. Fig. 25 shows the predictive models for CF2 sections. It can be observed from Figs. 23-25 that the distributions of the residual stresses in the proposed models are similar in shape, though slight difference exists in the distribution of membrane residual stress near the welding seam. It was noted that the magnitudes of residual stresses at specific parts are different. The residual stresses are influenced by fabrication routes and are also dependent on the steel yield strength. More test results regarding the residual stresses in OctHSs are needed for future research to develop generalised predictive models.

4. Conclusions

The material properties and residual stress distributions in cold-formed octagonal hollow sections (OctHSs) have been investigated in this study. Two fabrication routes involving combined press-braking and welding were considered. A total of 46 tensile coupons extracted from parent plates and cold-formed OctHSs were tested. Strength enhancement up to 27% was observed at corners of cold-formed sections due to the cold-forming effect, while materials at flat portions exhibit similar responses to parent metals. The applicability of a predictive model for the strength enhancement in yield strength was assessed on a basis of 26 corner coupons extracted from OctHSs. Predictions from the model match well with test results yielding a mean prediction-to-test value of 1.03 with a corresponding CoV of 0.04. In terms of stress-strain curves, a new bilinear plus

nonlinear strain-hardening constitutive model was proposed for materials at flat portions, which can give satisfactory prediction in the strain-hardening range. As for cold-formed steel, an existing model was adopted to describe the stress-strain relationships at corners, which shows good agreements with test results. The magnitudes and distributions of longitudinal residual stresses in cold-formed OctHSs from different fabrication routes were also experimentally investigated. The maximum membrane and bending residual stresses were found to be up to 62% and 39% of the material yield strength. In terms of bending residual stresses, magnitudes in the flat regions were relatively low while magnitudes at the corners were much higher due to the cold-formed process. As for the membrane residual stresses, magnitudes near the welding seam were greatly larger than other locations. It was also noted that OctHSs fabricated from different routes exhibited different distributions and magnitudes of residual stresses. Simplified predictive models for the distributions of residual stresses in cold-formed OctHSs fabricated through different routes were proposed as well based on the test results.

Acknowledgement

The research work presented in this paper was supported by a grant from the Research Grants Council of the Hong Kong Special Administrative Region, China (Project no. PolyU 152492/16E). The authors also appreciate the support from the Chinese National Engineering Research Centre for Steel Construction (Hong Kong Branch) at The Hong Kong Polytechnic University. The authors would also like to thank the technical staff, Mr. K.H. Wong, Mr. Y.H. Yiu and Mr. M.C. Ng, of the Structural Engineering Research Laboratory at The Hong Kong Polytechnic University for their assistance on the experimental works.

Reference

[1] J. Wardenier, Hollow sections in structural applications, 2nd ed. Geneva: CIDECT; 2011.
[2] T.M. Chan, L. Gardner, Compressive resistance of hot-rolled elliptical hollow sections, Eng Struct 30 (2008) 522-532.
[3] J.L. Ma, T.M. Chan, B. Young, Experimental investigation on stub-column behavior of cold-formed high-strength steel tubular sections, J Struct Eng, 142(5) (2016) 04015174.
[4] J. Wang, S. Afshan, N. Schillo, M. Theofanous, M. Feldmann, L. Gardner, Material properties and compressive local buckling response of high strength steel square and rectangular hollow sections, Eng Struct 130 (2017) 297-315.
[5] X. Lan, J. Chen, T.M. Chan, B. Young, The continuous strength method for the design of high strength steel tubular sections in compression, Eng Struc 162 (2018) 177-187.
[6] X. Lan, J. Chen, T.M. Chan, B. Young, The continuous strength method for the design of high strength steel tubular sections in bending, J Constr Steel Res 160 (2019) 499-509.
[7] CEN, EN 1993-1-1, Eurocode 3: Design of steel structures – Part 1.1: General rules and rules for buildings, Brussels, European Committee for Standardization (CEN); 2005.

[8] AISC, ANSI/AISC 360-16, Specification for structural steel buildings, Chicago, American Institute of Steel Construction (AISC); 2016.
[9] AISI, AISI S100, North American specification for the design of cold-formed steel structural members, Washington: American Iron and Steel Institute (AISI); 2016.
[10] A. Godat, F. Legeron, D. Bazonga, Stability investigation of local buckling behaviour of tubular polygon columns under concentric compression, Thin-Walled Struct. 53 (2012) 131-140.
[11] R. Gonçalves, D. Camotim, Elastic buckling of uniformly compressed thin-walled regular polygonal tubes, Thin-Walled Struct. 71 (2013) 35-45.
[12] R.M. Slocum, Considerations in the design and fabrication of tubular steel transmission structures. Proceedings of the fifteenth international symposium on tubular structures – ISTS 15, 27–29 May 2015, Rio de Janeiro, Brazil. 2015.
[13] A.T. Tran, M. Veljkovic, C. Rebelo, L.S. da Silva, Resistance of cold-formed high strength steel circular and polygonal sections-Part 1: Experimental investigations, J Constr Steel Res 120 (2016) 245-257.
[14] A.T. Tran, M. Veljkovic, C. Rebelo, L.S. da Silva, Resistance of cold-formed high strength steel circular and polygonal sections-Part 2: Numerical investigations, J Constr Steel Res 125 (2016) 227-238.
[15] W. Naohiro, I. Kikuo, O. Tadayoshi, K. Yosuke, Local buckling behavior of octagonal hollow cross-section member under axial compression or bending shear, ce/papers 1(2-3) (2017) 1116-1122.
[16] H. Fang, T.M. Chan, B. Young, Material properties and residual stresses of octagonal high strength steel hollow sections, J Construct Steel Res, 184 (2018) 479-490.
[17] J.Y. Zhu, T.M. Chan, B. Young, Cross-sectional capacity of octagonal tubular steel stub columns under uniaxial compression, Eng Struct, 184 (2019) 480-494.
[18] M. Sun, J.A. Packer, Direct-formed and continuous-formed rectangular hollow sections - comparison of static properties, J. Constr. Steel Res. 92 (2014) 67-78.
[19] K. Sefcikova, T. Brtnik, J. Dolejs, K. Keltamaki, R. Topilla, Mechanical properties of heat affected zone of high strength steels, Mater. Sci. Eng. 96 (2015), 012053.
[20] X. Liu, K.F. Chung, H.C. Ho, M. Xiao, Z.X. Hou, D.A. Nethercot, Mechanical behavior of high strength S690-QT steel welded sections with various heat input energy, Eng Struct 175 (2018) 245-56.
[21] R.B. Cruise, L. Gardner, Residual stress analysis of structural stainless steel sections, J. Constr. Steel Res. 64 (2008) 352-366.
[22] J.L. Ma, T.M. Chan, B. Young, Material properties and residual stresses of cold-formed high strength steel hollow sections, J Construct Steel Res 109 (2015) 152-165.
[23] CEN, EN ISO 6892-1:2016, Metallic materials– tensile testing. Part 1: Method of test at ambient temperature, Brussels, European Committee for Standardization (CEN); 2016.
[24] Y. Huang, B. Young, The art of coupon tests, J Constr Steel Res 96 (2014) 159–175.

[25] K.W. Karren, Corner properties of cold-formed steel shapes, J Struct Div, ASCE 93(ST1) (1967)401-432.
[26] ABAQUS/Standard. Version 6.13-1. USA: K. a. S. Hibbit; 2013.
[27] X. Yun, L. Gardner, Stress-strain curves for hot-rolled steels, J Construct Steel Res 133 (2017) 36-46.
[28] H.N. Hill, Determination of stress–strain relations from the offset yield strength values, Technical note No.927, Washington, DC: National Advisory Committee for Aeronautics; 1944.
[29] KJR Rasmussen, Full-range stress–strain curves for stainless steel alloys, J Constr Steel Res 59 (2003) 47-61.
[30] L. Gardner, X. Yun, Description of stress-strain curves for cold-formed steels, Constr Build Mater 189 (2018) 527-538.
[31] P.J. Withers, HKDH Bhadeshia, Residual stress: Part 1 — Measurement techniques. Mater Sci & Tech 17(4) (2001) 355-365.

Table 1. Test results of flat tensile coupons taken from parent plates.

Steel	$E_{s,p}$ (GPa)	v	$f_{y,p}$ (MPa)	$f_{u,p}$ (MPa)	$\varepsilon_{sh,p}$ (%)	$\varepsilon_{u,p}$ (%)	$\varepsilon_{f,25p}$ or $\varepsilon_{f,50p}$ (%)	$\varepsilon_{f,p}$ (%)
3 mm	209.5	0.28	546.5	625.8	2.2	10.9	27.1	26.0
6 mm	213.3	0.28	580.7	666.1	2.3	10.1	25.4	25.4

Table 2. Mean measured cross-sectional dimensions.

Specimen	Width, H (mm)	Side, B (mm)	Thickness, t (mm)	Outer radius, r_o (mm)	Inner radius, r_i (mm)	Side width, b(mm)	b/t
CF1-75×3	184.8	76.6	3.04	10.0	7.0	68.4	22.5
CF1-75×6	184.4	76.4	3.05	10.0	7.5	68.1	22.3
CF2-75×3	183.5	76.0	5.83	19.0	13.5	60.0	10.3
CF2-75×6	184.7	76.5	5.83	18.5	12.5	61.2	10.5

Table 3. Quarter-section tensile coupon test results of section CF1-75×3.

Coupon	E_s (GPa)	f_y (MPa)	f_u (MPa)	ε_u (%)	$\varepsilon_{f,25}$ (%)	ε_f (%)
W1	205.7	442.8	518.1	6.54	15.5	18.6
F2	211.5	549.8	620.0	8.97	23.6	25.5
F3	210.3	548.5	614.1	9.51	26.1	27.3
F4	208.4	543.0	618.6	10.84	26.5	27.0
F5	208.0	544.3	626.6	10.86	27.6	28.3
C6	200.6	661.1	696.2	1.26	10.5	16.3
F7	207.7	546.2	630.1	11.56	27.8	29.5
F8	209.1	545.7	624.5	11.03	27.2	29.0
F9	209.6	541.5	628.7	11.32	26.4	28.9
C10	202.8	661.4	690.0	1.07	-[a]	15.8

Note: a-For coupon C10 of CF1-75×3, fracture occurred outside the extensometer gauge length thus $\varepsilon_{f,25}$ was not obtained.

Table 4. Quarter-section tensile coupon test results of section CF1-75×6.

Coupon	E_s (GPa)	f_y (MPa)	f_u (MPa)	ε_u (%)	$\varepsilon_{f,25}$ (%)	ε_f (%)
W1	209.4	448.2	538.9	13.95	-[a]	26.9
F2	213.0	589.7	676.9	11.40	-[a]	29.2
F3	215.0	582.7	670.5	10.75	32.8	28.3
F4	213.5	580.0	666.0	10.74	30.5	27.7
F5	213.8	589.8	672.8	11.82	30.1	27.6
C6	200.5	730.6	776.3	1.44	14.3	14.1
F7	215.6	577.5	672.2	14.11	32.3	28.9
F8	214.3	577.3	671.1	11.10	30.2	28.8
F9	214.1	576.3	672.1	11.80	31.1	29.1

C10	198.9	732.8	770.2	1.26	13.3	14.6

Note: a-For coupons W1 and F2 of CF1-75×6, fracture occurred outside the extensometer gauge length thus $\varepsilon_{f,25}$ was not obtained.

Table 5. Quarter-section tensile coupon test results of section CF2-75×3.

Coupon	E_s (GPa)	f_y (MPa)	f_u (MPa)	ε_u (%)	$\varepsilon_{f,25}$ (%)	ε_f (%)
W1	206.2	453.1	532.7	7.91	16.8	23.2
F2	209.2	524.0	596.6	10.43	25.6	27.5
F3	212.7	541.6	611.3	9.75	24.1	25.6
C4	199.0	653.9	689.1	1.36	11.2	15.6
F5	211.8	538.8	621.8	10.96	26.7	28.4
F6	209.7	534.9	626.0	10.56	25.0	27.7
F7	209.2	539.6	634.3	11.90	27.8	28.8
C8	202.0	644.1	684.2	1.28	-[a]	15.8
F9	209.6	532.1	627.9	11.34	24.2	27.4
F10	209.7	541.4	636.9	11.87	25.2	28.0

Note: a-For coupon C8 of CF2-75×3, fracture occurred outside the extensometer gauge length thus $\varepsilon_{f,25}$ was not obtained.

Table 6. Quarter-section tensile coupon test results of section CF2-75×6.

Coupon	E_s (GPa)	f_y (MPa)	f_u (MPa)	ε_u (%)	$\varepsilon_{f,25}$ (%)	ε_f (%)
W1	207.7	459.8	541.7	9.15	-[a]	24.4
F2	210.4	568.9	647.1	11.40	22.1	27.1
F3	215.4	581.7	671.9	13.74	33.1	29.3
C4	196.6	737.7	778.3	1.32	14.7	14.7
F5	215.7	586.8	666.9	11.42	31.3	27.8
F6	214.9	580.3	669.2	11.74	30.8	27.6
F7	214.1	580.1	669.4	10.91	31.0	27.7
C8	196.6	738.9	779.0	1.32	14.5	14.1
F9	212.2	580.1	669.9	11.50	30.2	27.4
F10	212.8	582.6	671.9	10.95	-[a]	27.5

Note: a-For coupons W1 and F10 of CF2-75×6, fractures occurred outside the extensometer gauge length thus $\varepsilon_{f,25}$ was not obtained.

Table 7. Mean material properties for flat coupons taken from OctHSs.

Steel	$E_{s,f}$ (GPa)	$f_{y,f}$ (MPa)	$f_{u,f}$ (MPa)	$\varepsilon_{u,f}$ (%)	$\varepsilon_{f,25f}$ (%)	$\varepsilon_{f,f}$ (%)
3 mm	209.8	540.8	622.7	10.8	26.2	27.8
6 mm	213.9	581.0	669.1	11.7	30.5	28.1

Table 8. Mean material properties for corner coupons taken from OctHSs.

Steel	$E_{s,c}$ (GPa)	$f_{y,c}$ (MPa)	$f_{u,c}$ (MPa)	$\varepsilon_{u,c}$ (%)	$\varepsilon_{25,c}$ (%)	$\varepsilon_{f,c}$ (%)
3 mm	201.1	655.1	689.9	1.24	10.8	15.9
6 mm	198.2	735.0	775.9	1.33	14.2	14.4

Table 9. Corner coupon material properties for material models.

Steel	$E_{s,c}$ (GPa)	$f_{0.01}$ (MPa)	$f_{0.2}$ (MPa)	$f_{u,c}$ (MPa)	$\varepsilon_{u,c}$ (%)	Ma et al. [22]		Eq. (10)	
						n	m	n	m
3 mm	201.1	445	655.1	689.9	1.24	7.75	0.75	7.75	4.3
6 mm	198.2	499	735.0	775.9	1.33	7.74	0.80	7.74	4.3

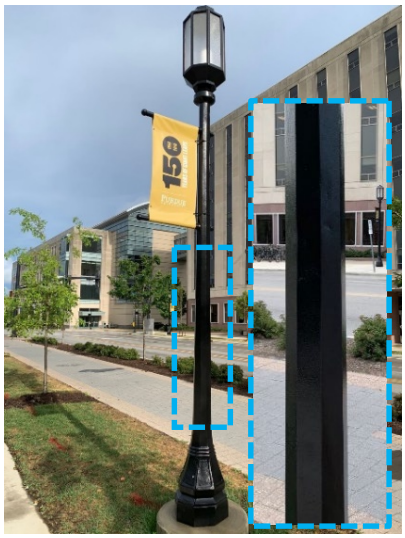

Fig. 1. Octagonal section lighting column (West Lafayette, US).

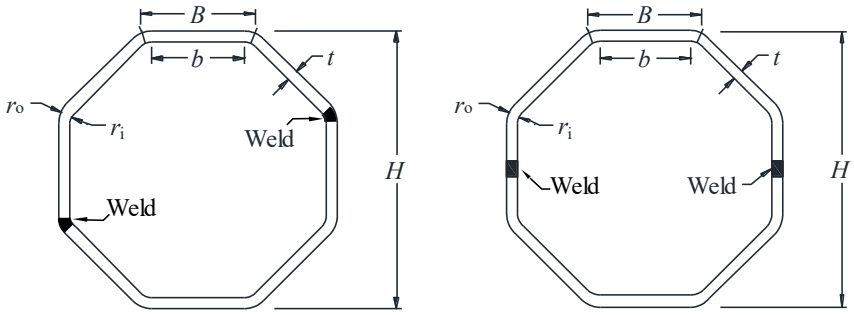

(a) CF1 (b) CF2

Fig. 2. Fabrication routes for octagonal steel hollow section.

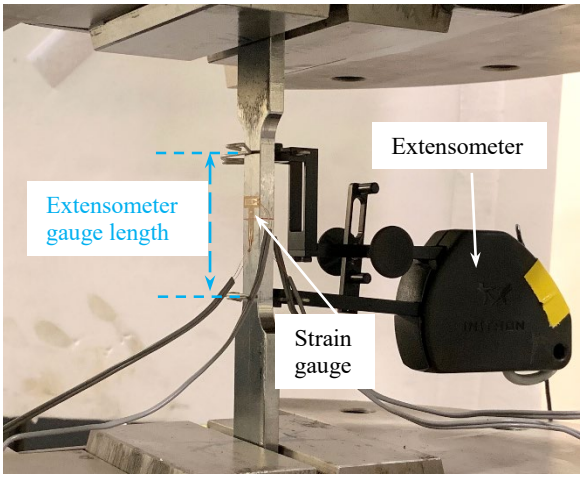

Fig. 3. Test arrangement of parent plate coupon.

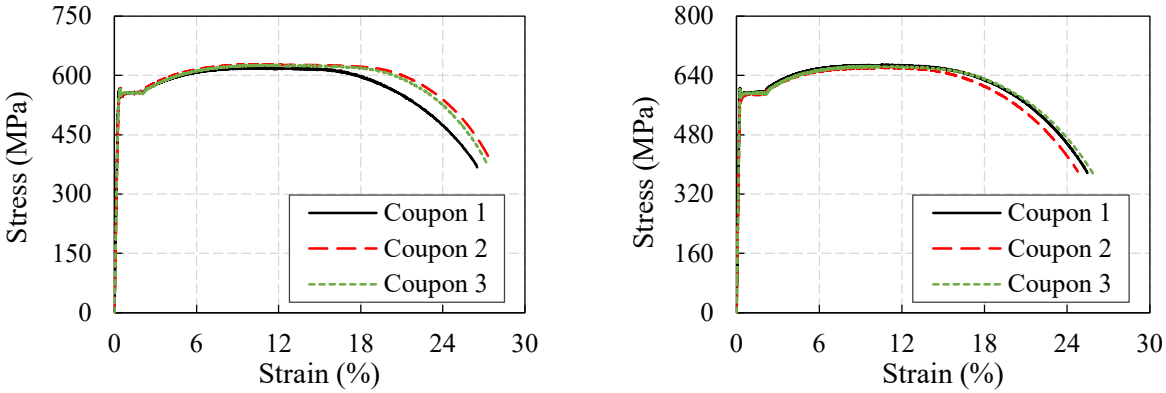

(a) 3 mm steel plate (b) 6 mm steel plate

Fig. 4. Stress-strain curves of the tensile coupons taken from parent plates.

(a) CF1 (b) CF2

Fig. 5. Locations of the tensile coupons taken from hollow tubes.

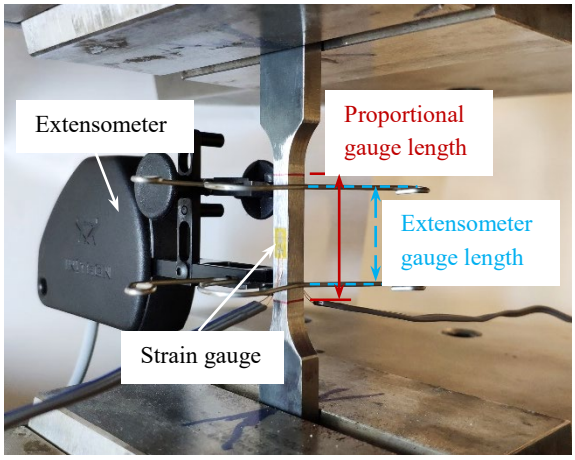

(a) Flat coupon tests.

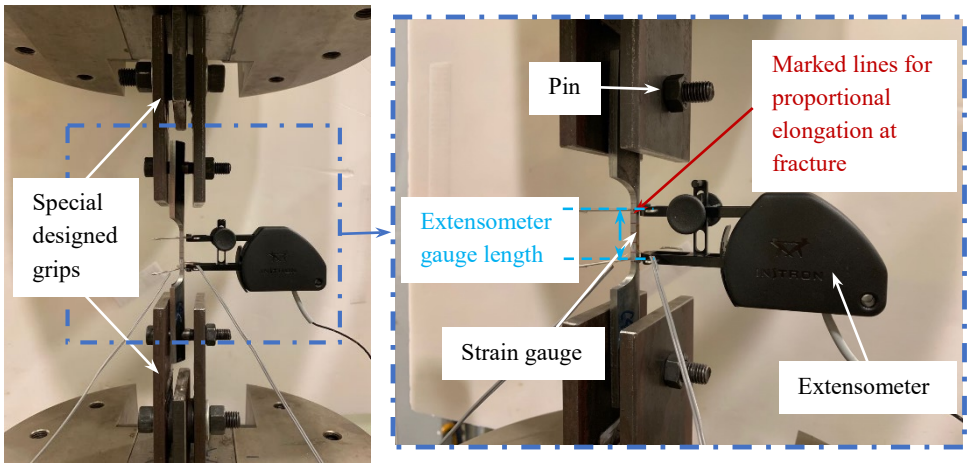

(b) Corner coupon tests.

Fig. 6. Test arrangement of flat and corner coupons extracted from quarter-section.

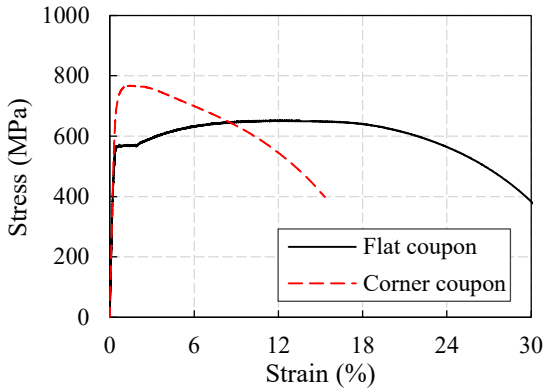

Fig. 7. Typical stress-strain curves of flat and corner coupons.

(a) Before test. (b) Failed specimens.

Fig. 8. Tensile coupons extracted from a quarter-section of CF1-75×3.

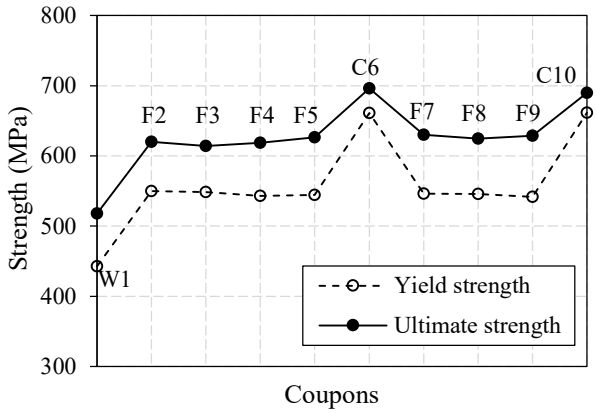

Fig. 9. Measured yield strength and ultimate strength distribution in CF1-75×3.

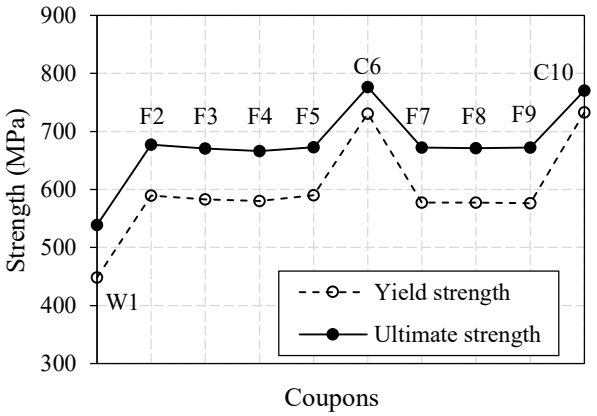

Fig. 10. Measured yield strength and ultimate strength distribution in CF1-75×6.

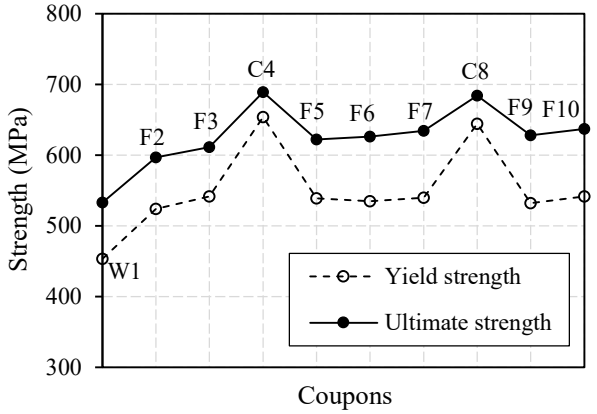

Fig. 11. Measured yield strength and ultimate strength distribution in CF2-75×3.

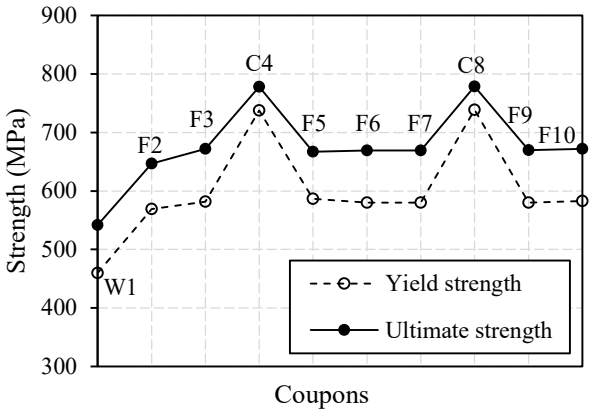

Fig. 12. Measured yield strength and ultimate strength distribution in CF2-75×6.

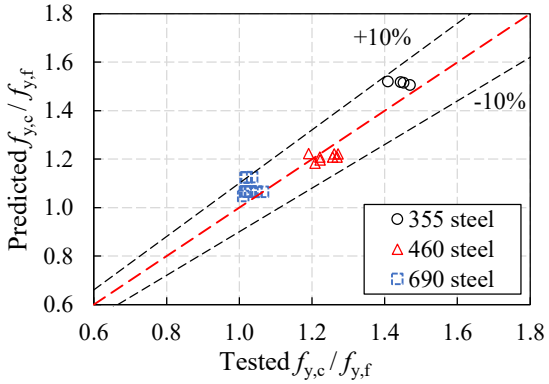

Fig. 13. Assessment of the strength enhancement predictive model.

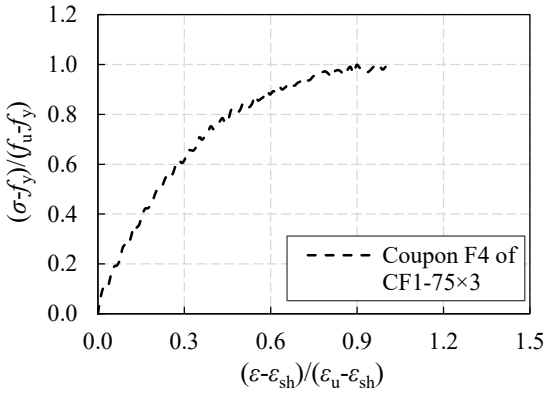

Fig. 14. Normalised nonlinear strain-hardening range of a flat coupon.

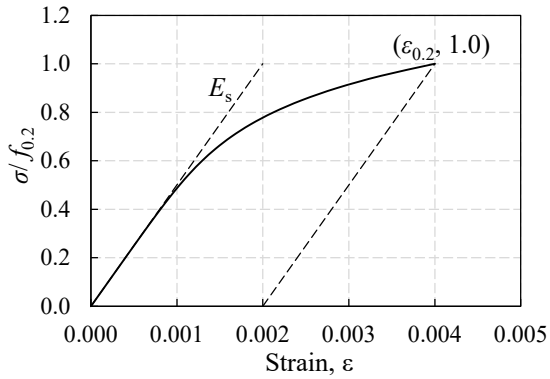

Fig. 15. Initial stress-strain curve of Ramberg-Osgood model.

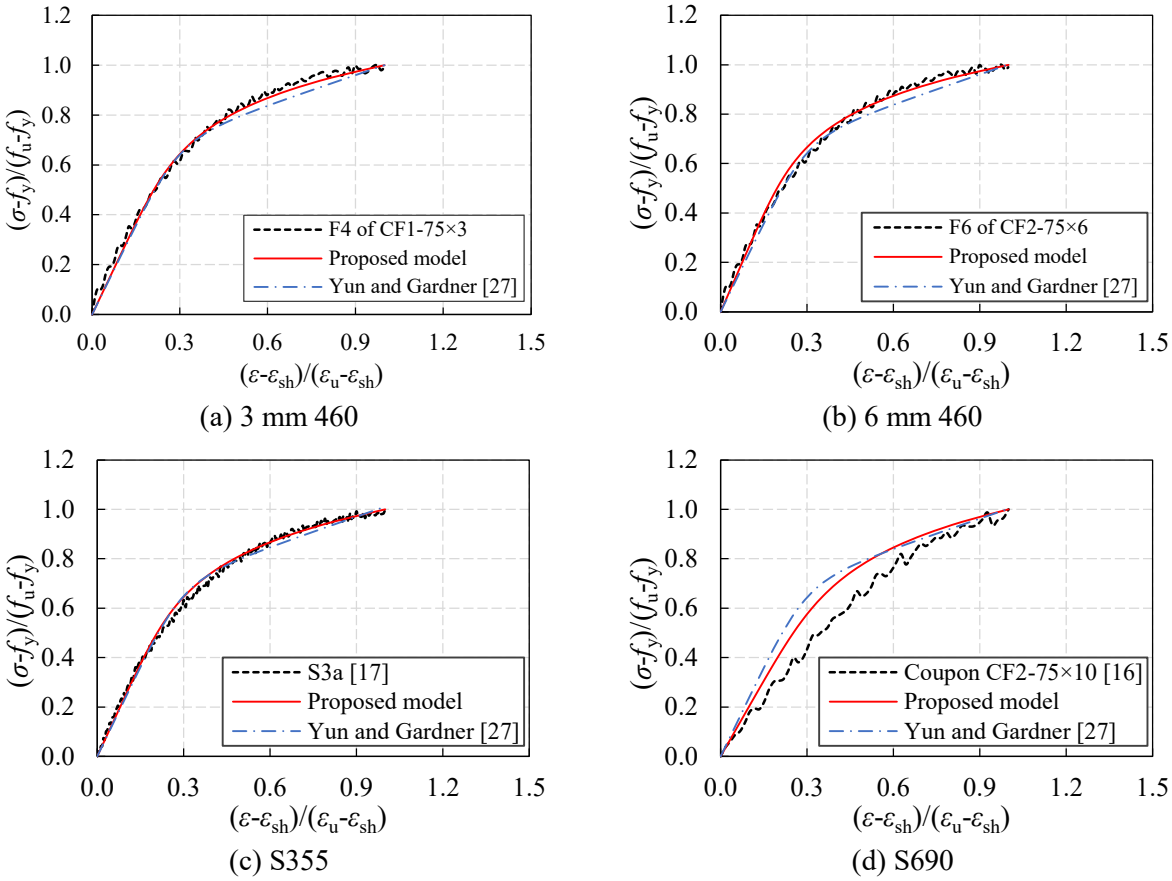

(a) 3 mm 460 (b) 6 mm 460

(c) S355 (d) S690

Fig. 16. Comparison of the proposed model with flat coupon test results (m = 6.0).

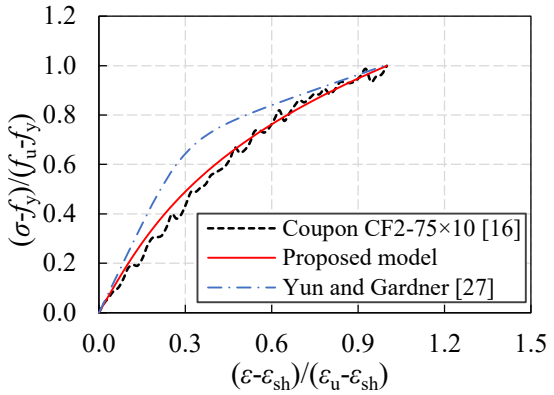

Fig. 17. Comparison of the proposed model with S690 flat coupon test results (m = 3.0).

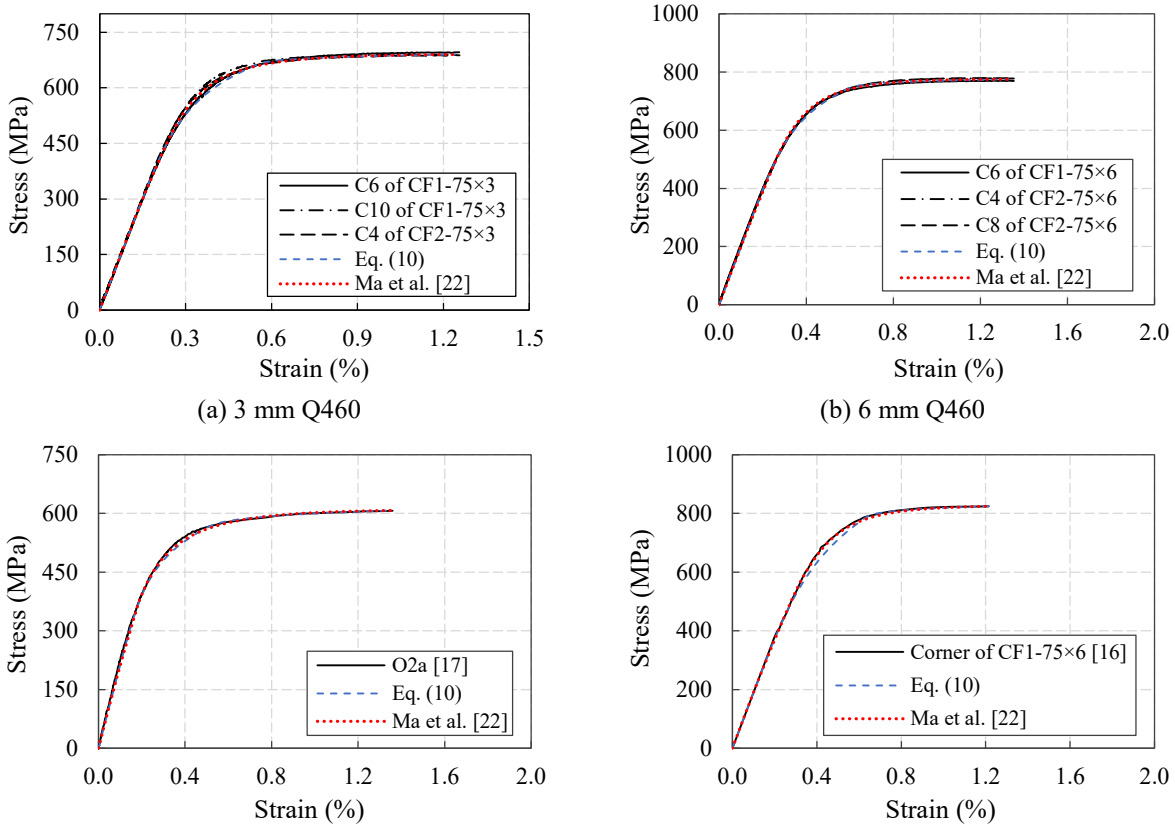

(a) 3 mm Q460 (b) 6 mm Q460

(c) S355 (d) S690

Fig. 18. Comparison of the predictive model with corner coupon test results.

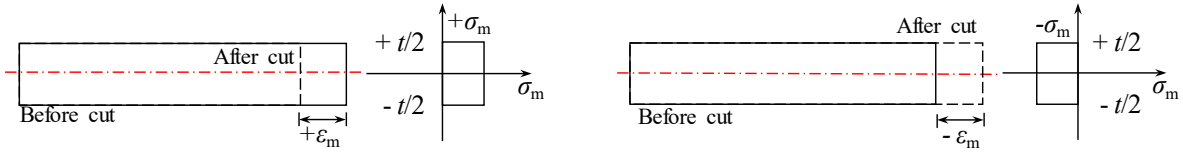

(a) Membrane residual stress σ_m acting in tension (b) Membrane residual stress σ_m acting in compression

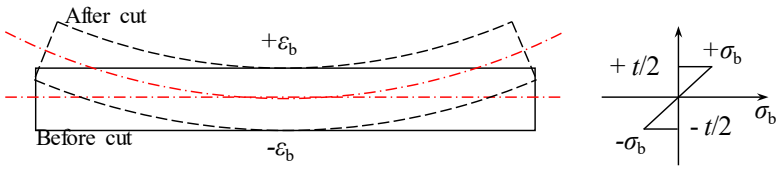

(c) Bending residual stress σ_b

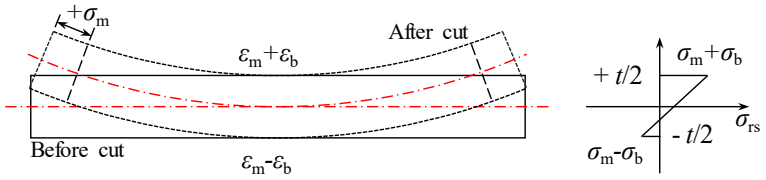

(d) Combined bending and tensile membrane residual stresses σ_{rs}

Fig. 19. Effects of membrane and bending residual stresses.

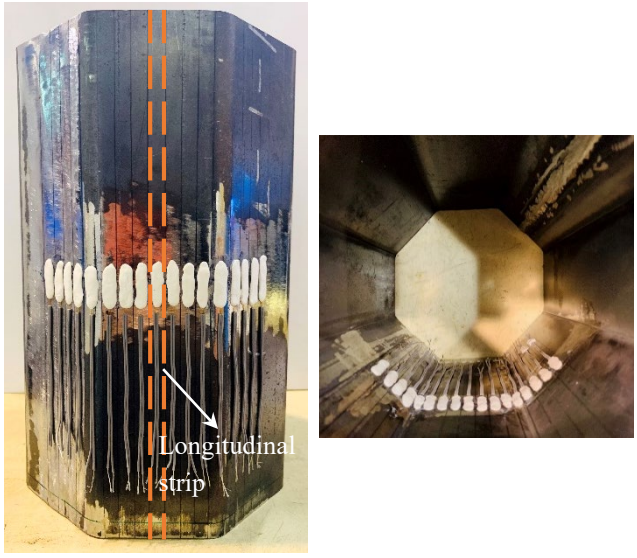

Fig. 20. Prepared specimen for sectioning (CF2-75×6).

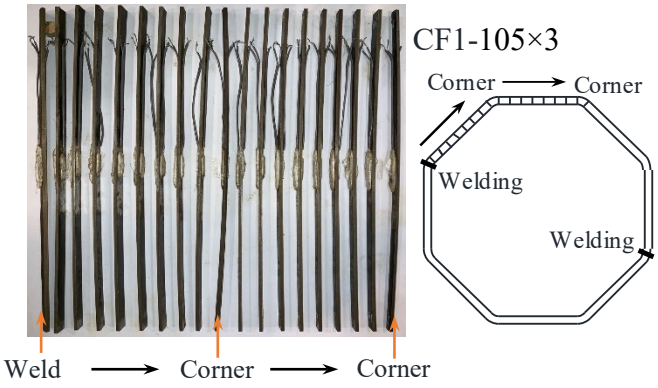

Fig. 21. Deformed strips extracted from CF1-105×3 after sectioning.

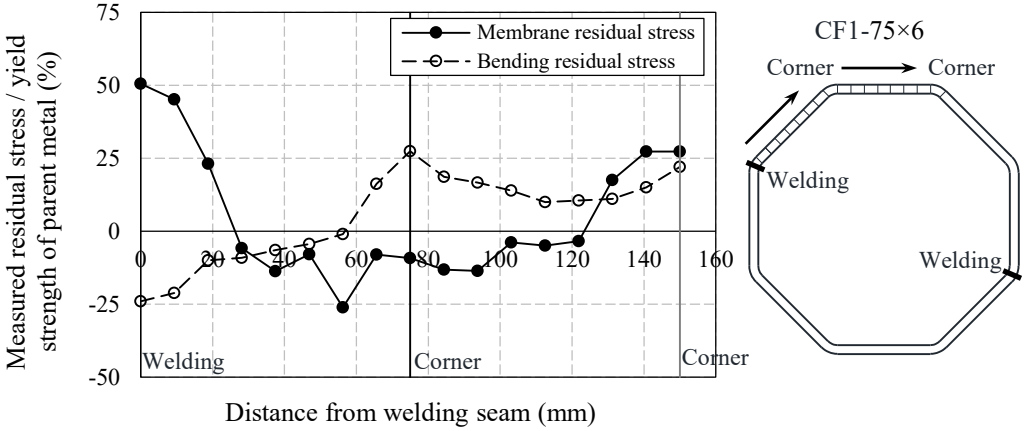

(a) CF1-75×6

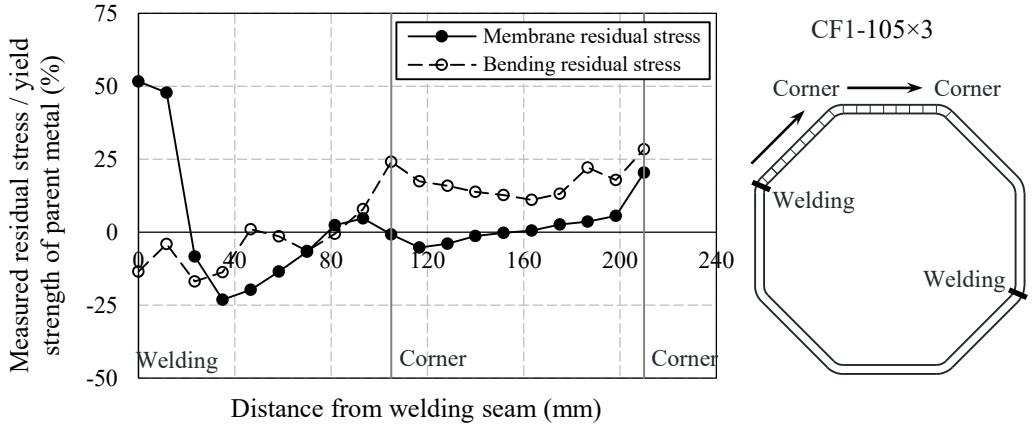

(b) CF1-105×3

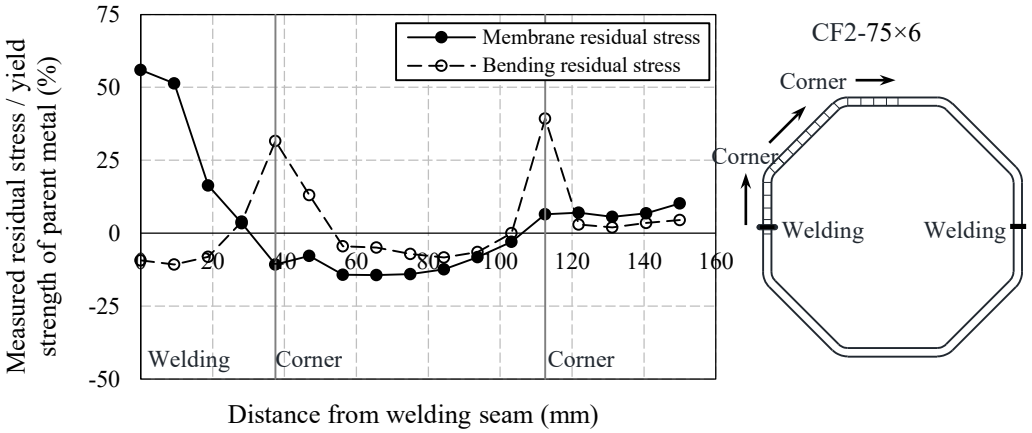

(c) CF2-75×6

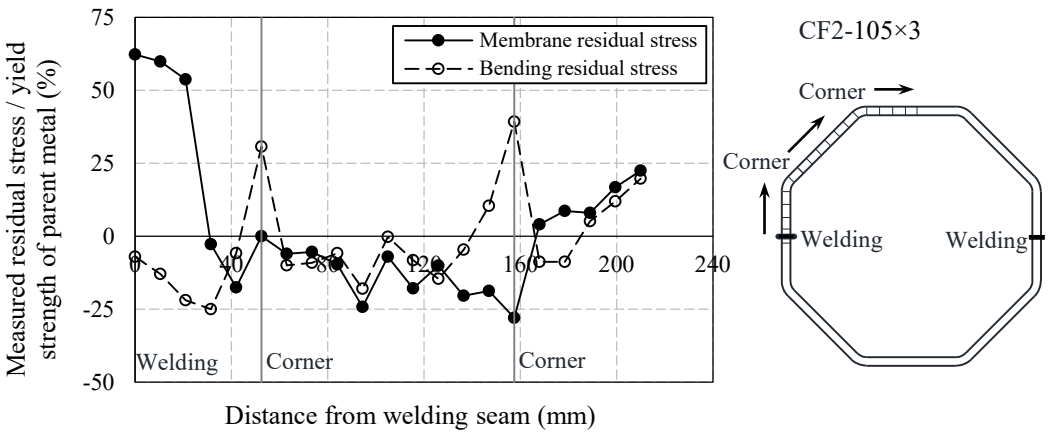

(d) CF2-105×3

Fig. 22. Longitudinal residual stress distributions of cold-formed OctHSs.

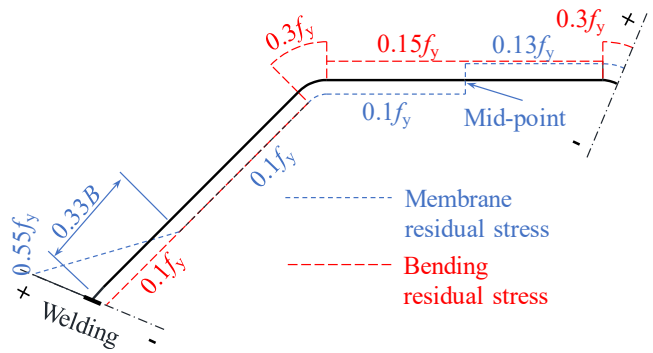

(a) CF1

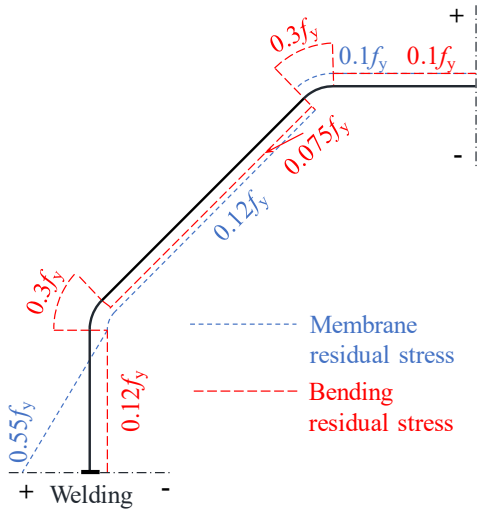

(b) CF2

Fig. 23. Predictive models for residual stress distributions in cold-formed OctHSs.

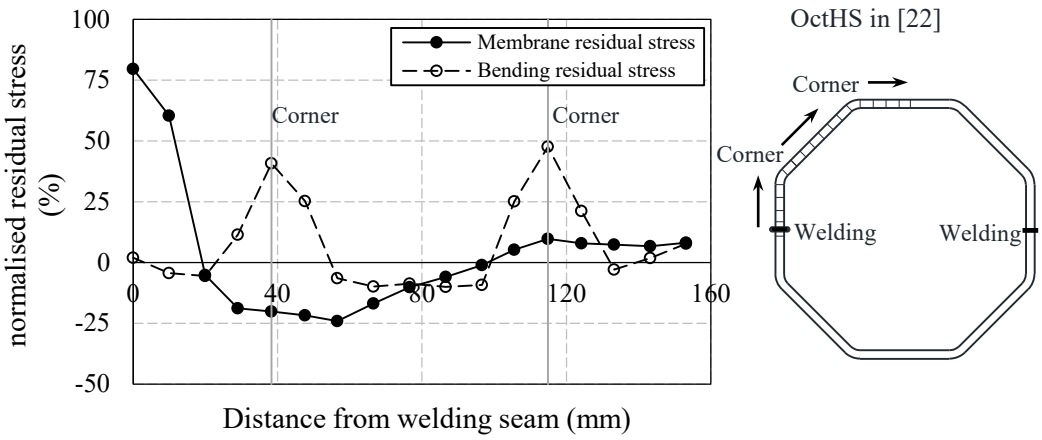

(a) Longitudinal residual stress distributions.

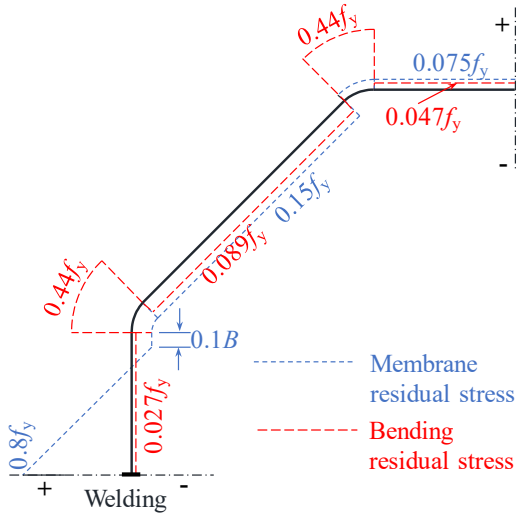

(b) Predictive models for residual stress distributions

Fig. 24. Longitudinal residual stress measurement in [22] (S355 steel).

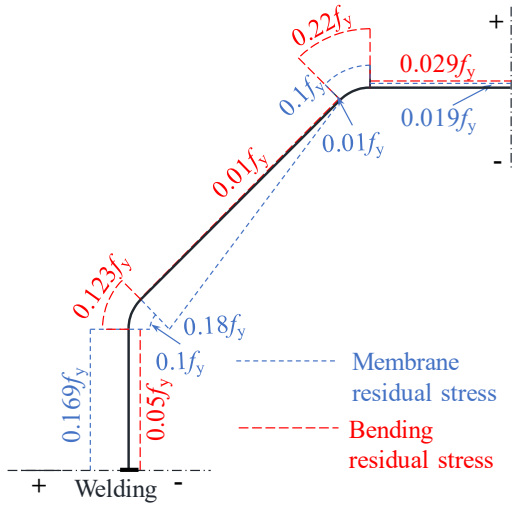

Fig. 25. Predictive models for residual stress distributions in [21] (S690 steel).